Surface & Coatings Technology 515 (2025) 132662

Contents lists available at ScienceDirect

Surface & Coatings Technology

journal homepage: www.elsevier.com/locate/surfcoat

Cathodic arc-deposited AlTiN hard coating tribology at elevated temperatures☆

Aljaž Drnovšek [a,*], Patrik Šumandl [a], Žan Gostenčnik [a,b], Janez Kovač [c], Miha Čekada [a]

[a] Jožef Stefan Institute, Department of Thin Films and Surfaces, Jamova 39, 1000, Ljubljana, Slovenia
[b] Jožef Stefan International Postgraduate School, Jamova 39, 1000, Ljubljana, Slovenia
[c] Jožef Stefan Institute, Department of Surface Engineering, Jamova 39, 1000, Ljubljana, Slovenia

A B S T R A C T

Cathodic arc evaporation (CAE) is the most commonly used physical vapor deposition (PVD) method to deposit protective coatings on cutting and forming tools. However, this deposition method results in a relatively rough surface due to micro-droplet emission. The first contact between the coating and the workpiece surface is at the sites of these growth defects, influencing the state of the contact, such as particle formation and oxidation spots. Growth defects significantly impact the coating's wear and friction properties. Their impact is not limited to the beginning of the contact formation but also expands in the long run, and they can deteriorate the coatings much sooner than expected. This research aims to monitor the wear and friction properties of the cathodic arc deposited AlTiN hard coating during the running-in and steady-state periods under different temperature conditions. Tribological tests against the Al_2O_3 counterbody were carried out at different temperatures, from room temperature up to 700 °C. The sliding distance at specific temperatures, ranging from 50 to 140,000 cycles, enabled us to monitor the wear progression from first contact formation at the growth defects to the complete coating wear from the WC-Co substrate.

After tribological tests, the samples were analyzed using detailed 3D profilometry, SEM, and FIB analysis to determine the wear mechanisms in different stages of high-temperature wear. Attention was focused on the growth defects, their impact on the running-in behavior, and the oxygen diffusion pathways along growth defects that ultimately lead to the delamination of the coating from the substrate.

1. Introduction

PVD hard coatings have consistently proven to be an effective solution for machining tools operating in demanding environments [1,2]. The adequacy of the coating performance is first tested in laboratory conditions, simulating as close to real conditions before the actual use of the coated tool. The entry point to test the wear and friction of the coating is by using a simple high-temperature (HT) ball-on-disc method in the laboratory. As in real applications, friction and wear first undergo the running-in period before the conformal contact between the coating and the counterbody occurs, and the tribological response is in a steady state of friction [3]. The running-in period depends mainly on the condition of the surfaces in contact. In general, topography (usually described in the surface roughness parameter) plays a crucial role in the length of the running-in period and its influence on the coefficient of friction (COF). Depending on the substrate material, deposition process parameters, coating material, or the deposition method used, coated surfaces can exhibit high differences in the final coating topography [4,5]. The deposition method plays a crucial role, as certain techniques, such as cathodic arc evaporation, often lead to very rough surfaces due to the continuous ejection of molten cathode material in the form of microdroplets that become incorporated into the coating. Cathodic arc evaporation (CAE) is frequently used for hard coatings deposition on cutting tools where the surface roughness does not play as big a role as in forming tools.

TiAlN is among the most popular coatings and the first one capable of withstanding high temperatures at the cutting edge. Adding Al to the TiN matrix improves the resistance to oxidation and wear, thus enabling higher cutting speeds [6–8]. Increased thermal load triggers self-hardening via spinodal decomposition, enhancing the hardness and wear properties [9–11]. The coating high thermal stability is based on forming a dense protective Al_2O_3 layer, which slows down oxygen diffusion into the coating [12]. Generally, a high Al content benefits the coating properties, but a balance in Al content is crucial to maintaining the desired properties, as excessive Al can alter the coating's structure [13–15]. As AlTiN-based coatings are arguably the most successful in wear protection of tools, they are also one of the most studied systems in the literature [7,16–19]. Different authors performed tribological tests at high temperatures with various Ti to Al ratios, showing increased COF with the temperature and slightly lower COF for coatings with higher Al

☆ This article is part of a Special issue entitled: 'ICMCTF 2025 (SCT)' published in Surface & Coatings Technology.

* Corresponding author.
E-mail address: aljaz.drnovsek@ijs.si (A. Drnovšek).

https://doi.org/10.1016/j.surfcoat.2025.132662
Received 11 June 2025; Received in revised form 23 August 2025; Accepted 9 September 2025
Available online 9 September 2025

content sliding against an Al_2O_3 counterbody [20]. Others showed that the COF decreases with the temperature sliding against the SiC ball but at relatively short tribological tests [21]. This suggests the complexity of a sliding contact at high temperatures where many mechanisms such as oxidation, mechanical changes of the coating and substrate, thermal stability changes, and many others overlay [22,23]. The chemical reactions on the surfaces are strongly influenced by the high local contact pressures and the flash temperatures, which can be over 1000 °C, at spots where asperities collide [24]. This effect can be even magnified in high-temperature environments and at rough, non-conformal contact, such as at the beginning of sliding at the running-in period. The latter was the focus of studies by several authors [25–28]. Our previous study focused on magnetron-sputtered TiAlN growth defects and their role in room temperature (RT) tribological contact with two typical test counterbody materials [29]. In the cathodic arc process, Tkadletz et al. investigated the effect of arc-evaporated droplets on the wear behavior of TiAlTaN coating [30]. He found that the droplet defects are crucial in coating crack formation at HT tribology. At the same time, Luo extensively studied the relationship between the COF and wear in the TiAlN/VN coating [25,31,32]. Fallqvist and Olsson analyzed VN-based coatings in detail regarding the influence of growth defects on mechanical and tribological properties [33]. They showed that the surface irregularities in coatings have a small impact on their overall strength but negatively affect their tribological performance in sliding contact. Growth defects at the substrate-coating interface significantly negatively impact the substrate-coating interfacial strength.

There is insufficient research on how wear characteristics change with test length and temperature for wear mechanism identification purposes. Previous studies have focused on the properties of AlTiN coatings, but there is a lack of research on how this coating behaves in terms of wear and friction at high temperatures. In the present study, our objective was to assess the wear and friction properties of the AlTiN coating during both the running-in and steady-state periods under varying temperature conditions. We conducted tribological tests at different temperatures, changing the test duration from 50 to 140,000 cycles, to see how the sliding test length affects the wear and friction of the coating.

We investigated the influence of wear debris generated mainly by breaking the growth defects at sliding contacts. The presence of these particles can significantly impact friction and wear differently, depending on the temperature. Detailed 3D profilometry, SEM, and FIB analyses were performed to determine the wear mechanisms at different stages of high-temperature wear. In addition, we conducted secondary-ion mass spectrometry (SIMS) studies to evaluate the extent of oxidation and identify different species present in the oxide layer. The combination of these analyses allowed us to understand the wear mechanisms and behavior of the arc-deposited AlTiN coating at high temperatures from the initial contact to the final coating breakdown. These new findings could provide significant benefits for cutting-tool applications as well as for coating research in general.

2. Experimental

2.1. Coating deposition

The AlTiN coating was deposited on cemented carbide (WC-Co) coupons using an industrial cathodic arc deposition system (Kobelco AIPocket, KCS Europe, Germany). Prior to deposition, the substrates were mirror-polished to a surface roughness of $S_a \leq 10$ nm and subsequently cleaned using a sequence of ultrasonic baths with solvents and deionized water, replicating the cleaning procedure employed for actual cutting tools.

During deposition, the test coupons were mounted on a planetary rotating holder, with a dual-axis rotation applied to ensure uniform coating distribution. The process commenced with 1 mPa base pressure, starting heating the samples to 450 °C under vacuum conditions, followed by an in-situ etching step (Ar atmosphere, 1 mPa) that removed several hundred nanometers from the top surface, eliminating surface contaminants. The AlTiN coating was deposited using four cathodes with a target composition of $Al_{60}Ti_{40}$ (99,9 % purity provided by KCS Europe), each operating at a current of 150 A for 45 min in a pure nitrogen atmosphere at a pressure of 4 Pa. The bias on the table was -70 V DC.

2.2. Coating characterization

The thickness of the coating was measured using the ball crater method (Calotest). Additionally, the adhesion of the coating was evaluated by Rockwell-C indentation and Scratch tester (CSM) using a diamond tip with a radius of 200 μm. 3D stylus profilometry (Dektak XT from Bruker) and scanning electron microscopy (FEI, Helios Nanolab 650) equipped with an ion source for cross-sections were used to characterize the coatings and the tribological products. Simultaneously, an energy dispersive spectroscopy (EDS) was performed on both wear tracks and pristine coatings. X-ray diffraction (XRD) was conducted on several coatings before and after the HT tribology using Bruker AXS D4 Endeavor. The hardness of the coating was measured with a Vickers diamond indenter (H100C, Fisherscope). The indentation measurements were analyzed using the Oliver-Phar method. Time-of-Flight Secondary Ion Mass spectroscopy (ToF-SIMS) (model TOF.SIMS 5, ION-TOF, Germany) was used to determine the thickness of oxide on the wear scar and on the pristine sample. ToF-SIMS analyses were performed using a bismuth liquid metal ion gun with a kinetic energy of 30 keV. The SIMS spectra of negative ions ($AlO2^-$, AlN^-, TiO^-, O^-AlNO^-) were measured by scanning a Bi+ ion beam over area of 100 × 100 μm2 in size. SIMS depth profiles were performed in dual beam depth profiling mode using the 1 keV Cs+ ion beam rastering over 0.4 × 0.4 mm for sputtering. Etching rate was estimated to be 0.06 nm/s.

2.3. Tribology

We used a high-temperature ball-on-disc tribometer (Anton Paar) in a rotating configuration for tribological characterization. Tribological experiments were performed in an air atmosphere at room temperature at a 5 mm radius, at high temperatures (250, 500, and 700 °C) at a 4 mm radius. Al_2O_3 ball (6 mm radius) was used as a counterbody due to its inertness and relatively high hardness at high temperatures. The normal force on the surface was set constant for all experiments at 2 N. The length of the test was moderated so that friction and wear coefficient could be determined at running-in (100, 300, 500, 1000, and 2000 cycles) and steady-state (5000, 10,000, 30,000, 70,000, 140,000 cycles) periods. The linear velocity was kept steady at 18 cm/s.

The wear rate was estimated from 3-D profile images. The peaks belonging to protrusions (e.g. growth defects) are several hundred nm above the level of the coating. They were accounted for in the measurement by analyzing 500 line profiles simultaneously. During the coating deposition, the growth of defects occurs spatially localized and sporadic. Therefore, samples from the same batch differ slightly in defect density.

3. Results

3.1. Coating properties

Before the high-temperature tribological tests, the coated samples were thoroughly evaluated. Uniform deposition resulted in the formation of s AlTiN coating with a thickness of approximately 4 μm on all tungsten carbide coupons (Supplementary S1a). Samples were subjected to 3D profilometry to determine the average number of growth defects on the surface. The CAE deposition process produced significantly higher growth defect density than coatings deposited by magnetron sputtering. While the surface density of growth defects in AlTiN coatings

prepared by magnetron sputtering is a couple of hundred defects per mm^2 [34], in CAE coatings, it is at least ten times higher. The defect count varies among samples; however, no significant differences were observed overall. On average, the samples exhibited approximately 2500 ± 350 defects per mm^2. Minor spatial variations (±100 defects) within individual samples were also detected. The difference in defect density arises from the deposition process itself. In magnetron-sputtered coatings, defects typically originate from seeds formed by the substrate material, coating chipping, or foreign particles. In contrast, the CAE process continuously emits the target material in the form of droplets. Consequently, the seed composition is generally similar to that of the target. However, because droplet emission is continuous and sample rotation is applied, the resulting defect density across the samples is not completely uniform. Defects also vary in geometry. Some defects can reach up to 1.5 μm in height, while most are below 1 μm. SEM imaging further revealed that the coatings deposited by cathodic arc show rough surfaces continuously interrupted by various-sized droplet defects, protrusions, and small pits (Fig. 1b). Microdroplets on the surface that are emitted during the CAE process only poorly adhere to the coating matrix, and due to high compressive stresses, some of them are pulled out during deposition or after it, leaving cavities (pits, depressions) in the coating. In the STEM image (Fig. 1c) obtained from the SEM microscope, a dense columnar structure with an average column width of approximately 200 to 300 nm is observed for this coating.

The structure and mechanical properties of the coating were examined before and after high-temperature tribological tests. X-ray diffraction (Fig. 2a) shows that the as-deposited coating exhibits a cubic crystal structure with a predominant (200) orientation. No hcp-AlN phase was found in as-deposited coatings with an average composition of $Al_{28}Ti_{22}N_{50}$. This is maintained even after annealing at 700 °C as the decomposition process is expected at a higher temperature [35]. A shift of the (200) peak toward cubic TiAlN can be observed after HT annealing, simultaneously with a broadening of the (111) peak. The latter could be due to thin oxide formation on the coating surface as there are peaks for TiO_2 and w-type AlN in the vicinity. A slight shift of (200) to higher angles (by 0.18) could be due to recrystallization, stress relaxation, and dislocation rearrangement in the coating [36,37]. The calculated crystallinity size from the (200) peak does change from 10.8 nm in the as-deposited state up to 12.5 nm after the 700 °C tribological test.

Depending on the sample, the AlTiN coating hardness values were between 3400 and 3600 HV with an E-modulus of around 350 GPa in the as-deposited state (Supplementary S3). This yields H/E ≈ 0.1 at room temperature. The combined effect of elasticity and hardness is regarded as a reliable indicator of wear resistance. A higher H/E ratio in a coating suggests an enhanced ability to resist mechanical degradation and failure under tribological contact, as the contact area can remain elastic under higher stresses during external impacts. The change in H/E with increasing temperature for these samples was not measured, but it is expected to decrease similarly to other reports, reducing the coating wear capabilities [38]. A room temperature hardness after annealing at 700 °C decreased, presumably due to some stress relaxation and thin oxide layer on the surface that grew during the HT tribological test.

The coating adhesion was measured by Rockwell C indentation (Supplementary S1b) and a scratch test (Supplementary S2). Both tests showed good adhesion of the coating to the WC-Co substrate as the total delamination force on the as-deposited coating was around 124 N (Fig. 2b). After the HT tribological test the critical load also experienced a reduction. Similarly, the coating adhesion reduction with the increased temperature was measured on a typical hot work tool steel [39]. In our tests after 700 °C annealing, the coating completely delaminated at 107 N, nearly 20 N less than the force required for the as-deposited sample.

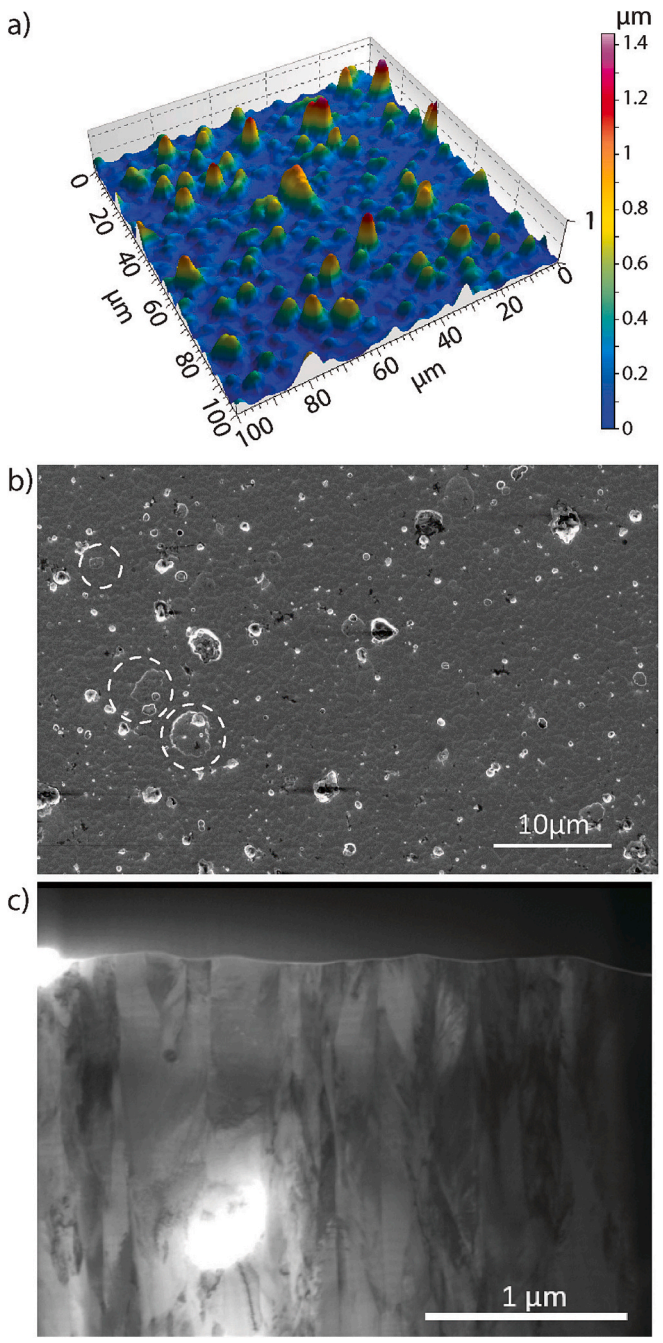

Fig. 1. (a) The 3D-profilometry image of a typical CAE deposited AlTiN coating. (b) SEM top view image of the coating surface. The surface consists of micro-droplet defects and small pits (encircled), i.e., where micro-droplet defects were ejected from the surface during or after deposition; (c) STEM image of an AlTiN cross-section.

3.2. Friction and wear rate measurements

Fig. 3 shows average friction coefficient measurements in (a) and wear rate in (b). In the top graph, each dot represents the average friction coefficient for individual measurement. As an example, the longest full measurement is added as a line at a specific temperature.

When an AlTiN coating forms contact with an Al_2O_3 ball at room temperature (Fig. 3a), the initial friction coefficient is around 0.6 for the first 50 cycles. Then, the friction coefficient increases significantly, reaching a peak of 1.05 at the end of the initial 2000 cycles. From cycle 2000 to 10,000, the friction stabilizes and stays around 1. After 15,000

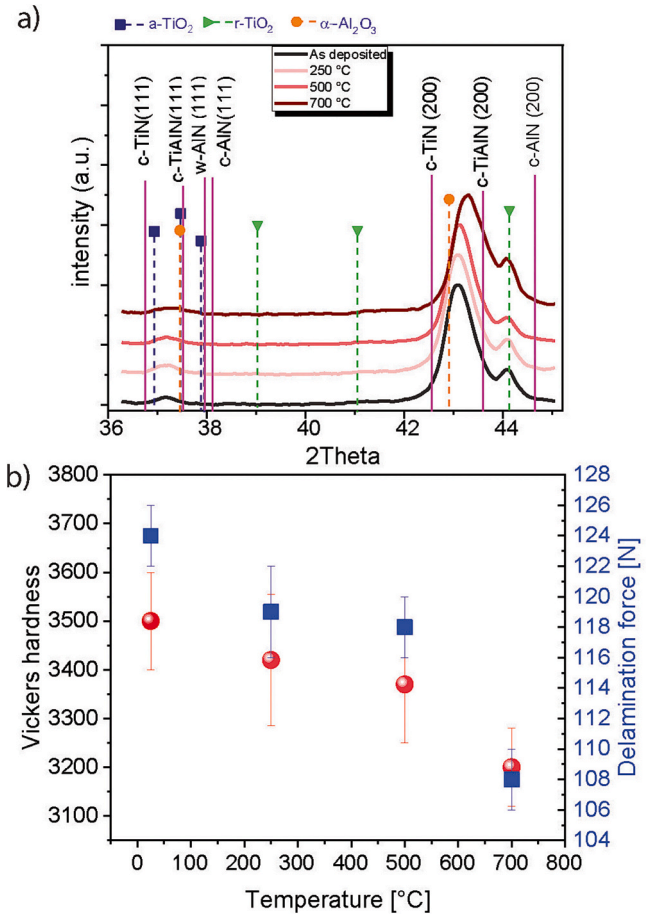

Fig. 2. (a) X-ray spectra for TiAlN coating after deposition and after HT tribological tests; (b) average hardness (red) and critical load of total delamination in the scratch test are shown. (For interpretation of the references to color in this figure legend, the reader is referred to the web version of this article.)

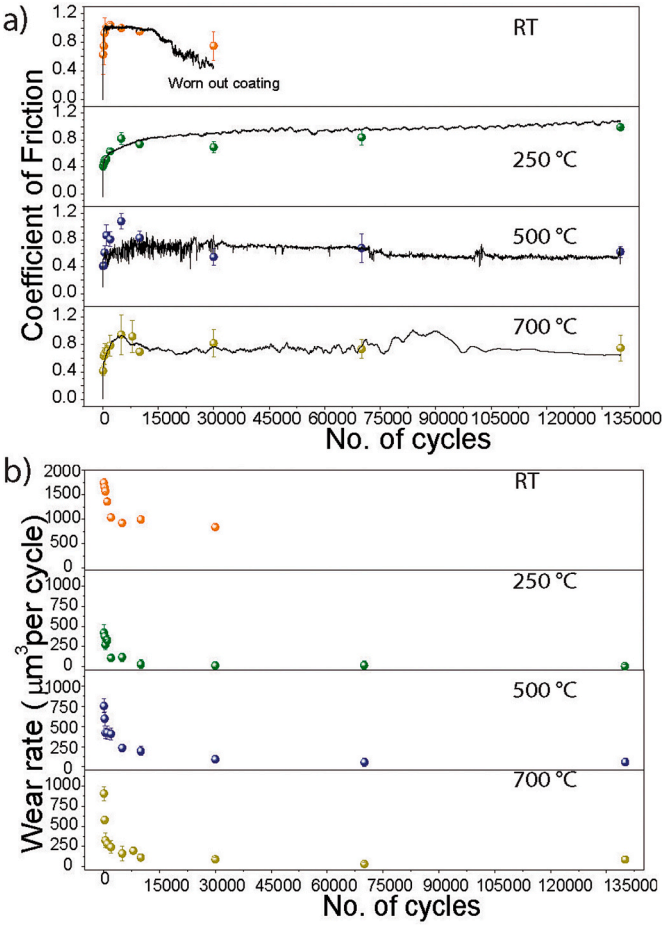

Fig. 3. (a) The average friction coefficient at different sliding distances measured at RT, 250, 500, and 700 °C, line at each graph is an individual measurement at maximal test length; (b) the average wear rate for corresponding COF measurements.

cycles, the friction starts to decrease, and after about 18,000 cycles, the friction becomes less consistent, with scattered values. This behavior indicates that the coating is progressively removed, and the COF measurement evaluates substrate material.

At 250 °C, the initial COF is 0.4. Over time, COF gradually increases with the number of cycles, taking about 2000 cycles to reach 0.6. During the running-in period, the maximum COF observed is 0.8 after 5000 sliding cycles. After 10,000 cycles, the COF stabilizes at approximately 0.7, marking the end of the initial running-in period. The test was extended to 140,000 cycles, during which the COF value gradually rose from 0.7 to about 1.0 by the end of the test. This final value is comparable to the results obtained from the RT tests. The complete measurement over the 140,000 cycles, represented by the black line, aligns well with the individual measurements. The data is consistent and shows a gradual increase in the coefficient of friction until it reaches the value of 1.0.

Similar to the 250 °C test, at 500 °C, the starting COF value is 0.4 for the short-term measurement. The friction then quickly increases up to 1.1 after 5000 cycles. This presents a maximal friction coefficient. It starts to decrease to 0.85 at 10,000 cycles and stabilizes at 30,000 cycles at 0.55. The COF fluctuates around 0.6 with a further increase in the number of cycles. The running-in period at this temperature is much more extended than at RT and 250 °C. The results of tribological tests conducted at a temperature of 700 °C revealed that after 100 cycles, the COF was approximately 0.4. However, this value increased to 1 after 5000 cycles, with the highest friction value recorded after 2000 cycles. After 10,000 cycles, the COF value decreased to 0.7. Tests performed at temperatures ranging from 30,000 to 140,000 showed an average COF of about 0.8. It was noted that the tests conducted at higher temperatures exhibited more scattered values compared to those carried out at lower temperatures, as indicated by the error bars and a complete sample test at 140,000 cycles.

The wear rate measurements for all tests are presented in Fig. 3b. Generally, the wear rate is high at the beginning of the sliding process. As the alumina counterbody comes into contact with the asperities of the coatings, these asperities break under the high Hertzian pressure (Fig. 4a). The wear rate gradually decreases until all asperities are leveled up and a stable contact zone is formed between the bodies in contact. The mechanical properties of the contacting bodies significantly influence the wear and friction characteristics of the system, which vary considerably with the testing temperature. At room temperature, the wear rate is highest at the onset of sliding. During this running-in period of low friction, wear is at its maximum, reaching approximately 1750 μm^3 per cycle. Conversely, as the friction increases, the wear rate decreases.

After the running-in period, the wear rate declines to a value of about 1000 μm^3 per cycle (after 2000 cycles), which is maintained throughout the steady-state friction period. Similarly, at 250 °C, wear is the highest at the beginning of the sliding tests. However, the measured wear is significantly lower than in the RT tests. The maximum wear is 430 μm^3 per cycle in the first 50 cycles. With longer tests, the wear drops to about 20 μm^3 per cycle after 10,000 laps. The wear remains minimal in steady-state friction, between 5 and 15 μm^3 per cycle. The maximum depth of

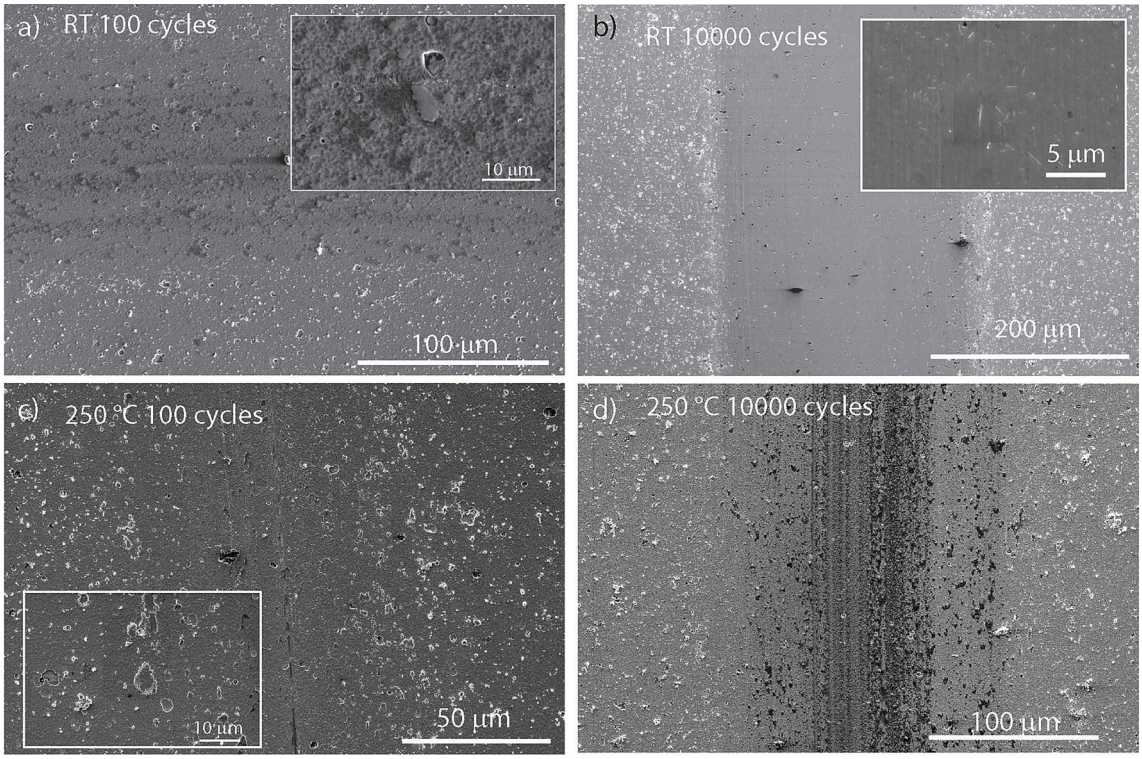

Fig. 4. The wear track after 100 cycles (a) and after 10,000 cycles (b) at RT. Roll-like debris is are visible in the inset. In c) the wear track after 100 cycles and in (d) after 10,000 cycles at 250 °C.

the wear scar at 140,000 cycles was only around 200 nm. At 500 °C test the measurements show a similar behavior as the lower temperature tests. The wear is the highest (750 per cycle) at the beginning of the sliding when the contact between the alumina ball and the coating surface is not conformal. The wear is decreasing with the test length, but it takes about 30,000 cycles to reach steady values. These fluctuate around 60 μm^3 per cycle. At 700 °C, the wear rates experience a maximum of 950 μm^3per cycle in the first cycles. However, as the test duration increased, wear decreased and reached stable values after 30,000 cycles, fluctuating around 90 μm^3per cycle. The results indicate that wear attains its maximum at room temperature, reaches a minimum at 250 °C, and subsequently exhibits only a slight increase with further temperature elevation.

3.3. SEM and EDS analysis of the wear tracks

The SEM images in Fig. 4 show the wear track at different sliding distances at room temperature and at 250 °C. Low friction and high wear can be attributed to breaking the growth defect tops during the first few cycles of the running-in period (Fig. 4a and c). As these defects are the first contact points, the contact area is minimal, and the pressure from the ball on these points is high. This causes the breaking of these asperities, creating a larger contact surface area and a large amount of wear debris in the contact region.

The figures show that the coating surface is unaffected by the sliding in the first 100 cycles; only the asperities are deformed, while the fragments of broken nodular defects are scattered near the defect, seen in both insets in Fig. 4a and c. With further sliding, the asperities are gradually leveled with the coating surface. The debris is collected along the outer edges of the wear track. This process is gradual, and as the wear track widens, more of the asperities are subjected to this process. Hence, the slow increase in contact area causes an increase in friction. As the number of cycles increases, the wear rate decreases.

The wear track after 10,000 cycles (Fig. 4b) presents the stationary friction period at RT. The surface of the wear track is smooth, with only very shallow abrasion marks visible under high magnification. The surface contains roll-like wear debris and cylindrical-shaped 2D wear products up to a couple of hundred nanometers in length, as seen in the inset. This type of debris starts to emerge with the transition of friction from running-in to stationary friction period at about 2000 cycles.

At 250 °C, the wear tracks at the same number of cycles present different surface states. Similar to RT tests, the first contact points are formed at the highest asperities, nodular defects created by micro-droplet emission. These get suppressed under high Hertzian pressure, breaking down to form submicron particles. The SEM image in Fig. 4c shows that after 100 cycles, a shallow abrasion occurred in the wear track center with collected and smeared wear debris around growth defects (inset). This process of coating abrasion and growth defect leveling continues as the friction increases simultaneously. An SEM image (Fig. 4d) of the sample wear track after 10,000 cycles reveals that the wear track is covered with abrasion marks at the peak of running-in period.

Wear track investigation also reveals some shallow delamination or spallation accrues of the top coating surface around defects (Fig. 5a circled). This process also creates the wear debris which is collected in small depressions in the wear track. They can accumulate to about 100 nm thick, while the wear track itself is covered with a few nm of oxidized coating. Inspection of the wear track after 30,000 to 140,000 cycles shows a gradual smoothing of the wear track (Fig. 5b). The cavities are visible on the spots of growth defects. The wear rate is more constant in this sliding period due to the smooth oxide tribological layer formed on top of the coating.

In Fig. 6, SEM images reveal the wear surface after 500 °C and 700 °C tests. After 100 cycles, the asperities are squashed and leveled with the coating surface in the middle of the wear track. As seen from the inset on the left in Fig. 6a, this process does not generate a lot of free wear debris but smears the oxidized asperities over the wear track area. At maximum friction, 5000 cycles, the wear track appears heavily oxidized with severe abrasion marks in the oxidized coating (Fig. 6b). The coating is covered with TiAl-oxide material, and it appears damaged under the

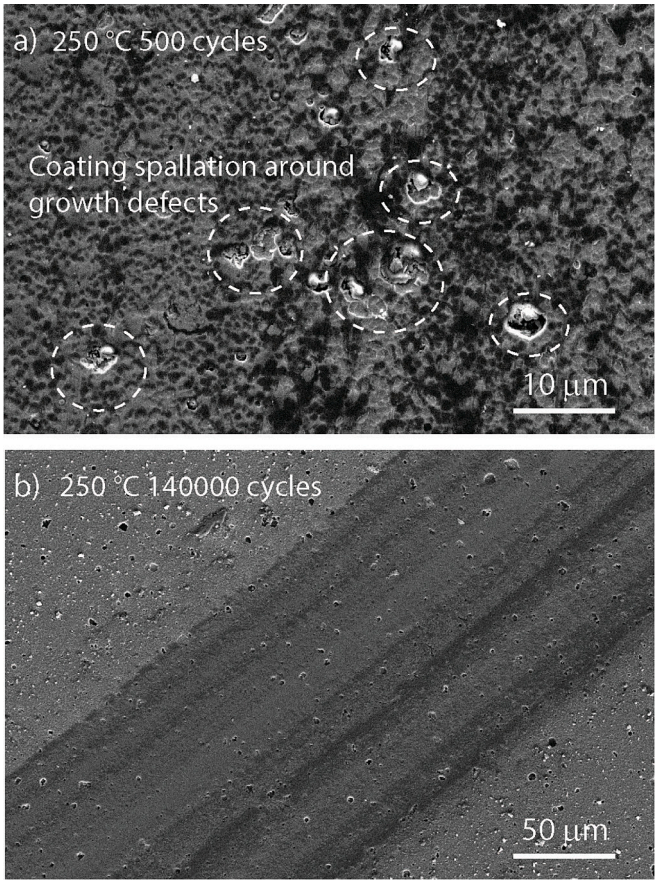

Fig. 5. (a) High magnification of the wear track at 250 °C after 500 cycles. Coating spallation is visible around growth defects. In (b), wear track after 140,000 cycles at 250 °C.

abrasion marks, as shown in the FIB cross-section (inset in b). In contrast to lower temperature sliding, the wear track at 500 °C does not experience smoothing in long sliding distances (Fig. 7). The wear track after 140k cycles is fully oxidized and covered with abrasion marks. Small voids and chippings on the top of the coating appear between those micros-sized cracks. A FIB cross-section in this region shows that the material oxidized along these cracks.

SEM images in Fig. 6c and d showed that oxidation was crucial in all tests conducted at 700 °C. After 100 cycles, the wear track is oxidized, with defects broken off on the outskirts of the wear track and long abrasion lines outside the wear track center. The wear track was much smoother after 10,000 cycles. From the FIB cross-section, it was observed that a uniform and dense oxide layer with a thickness of around 50 nm covered the entire wear track. As we increase the sliding length, the oxidative wear continues. After 70,000 cycles a smooth wear track is interrupted with several small spots of delamination. Further analysis (FIB cross-sections on Fig. 11b and c) showed that these delamination spots started at the side of defects. After 140,000 cycles, the coating delaminated at several places across the wear track, with patches of delamination several hundred micrometers in length. EDS mapping showed the tungsten oxide smeared on the top of the wear track (Fig. 8).

4. Discussion

Surface morphology has a strong influence on both the coefficient of friction and wear. Surface roughness and growth defect density do not only affect the COF and initial stages of wear, but they can also influence the overall performance of the tool, including chip formation, high-temperature abrasion, adhesion, and abrasive wear [40,41]. The experiments showed that the wear rate at a given temperature is not constant. The onset of sliding is characterized by the highest wear, after which the rate decreases with increasing sliding distance and eventually stabilizes once the running-in period is surpassed. This general trend is observed at all investigated temperatures; however, both the initial and

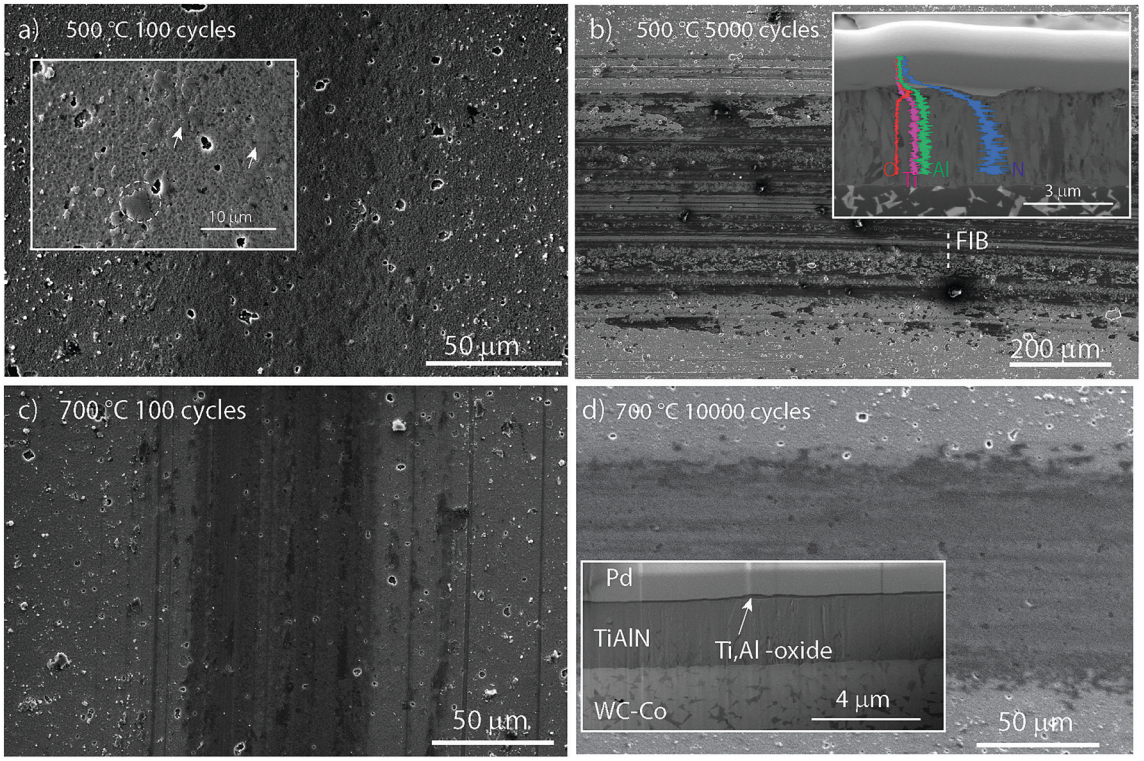

Fig. 6. The wear track after 100 cycles (a) and after 5000 cycles (b) at 500 °C. In c) the wear track after 100 cycles and after in (d) 10,000 cycles at 700 °C.

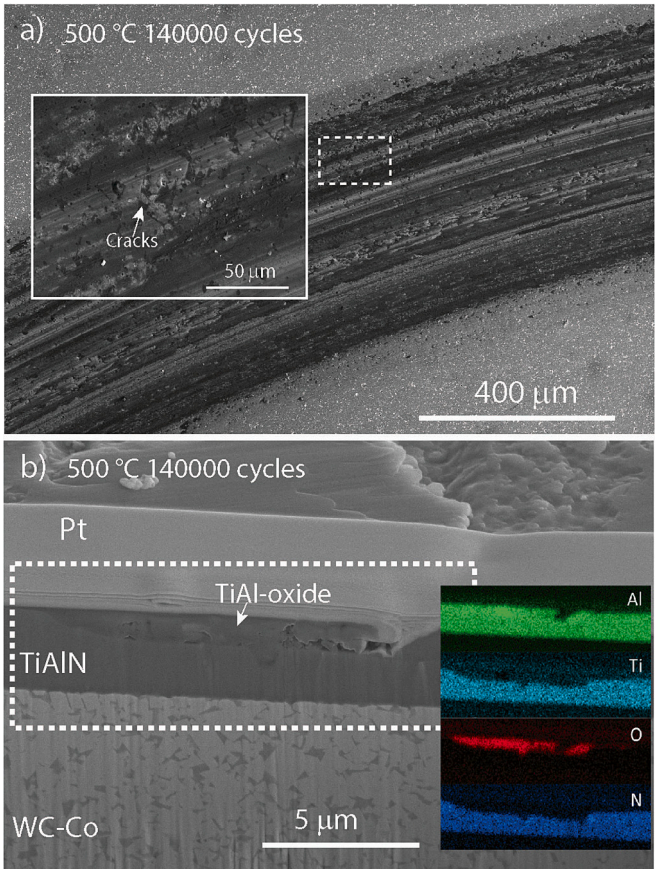

Fig. 7. a) The wear track after 140,000 cycles at 500 °C, an inset presents the magnification of the marked area. A FIB cross-section presented in (b) was made on the wear surface cracks.

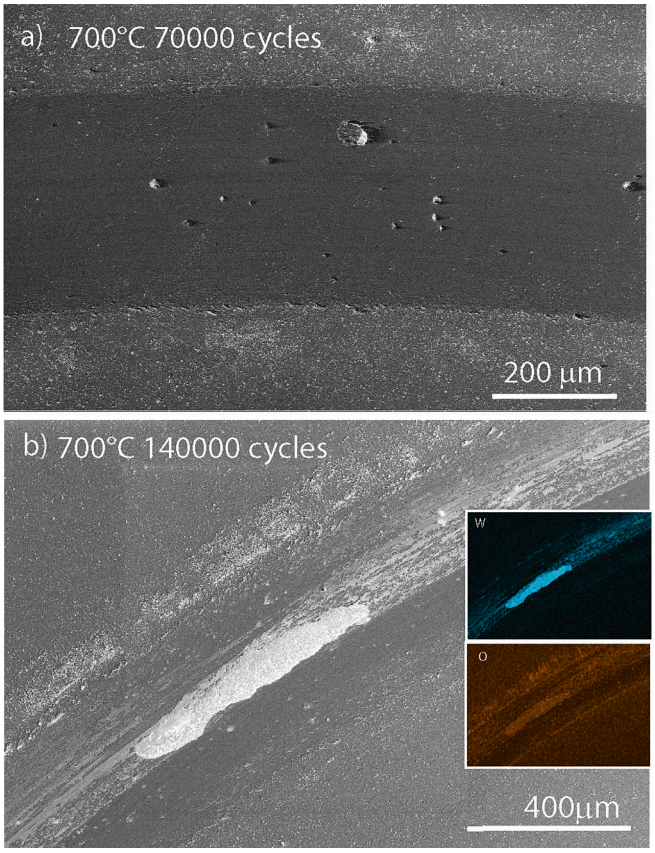

Fig. 8. The wear track at 700 °C after 70,000 cycles (a) and after 140,000 cycles (b), where large parts of a coating delaminated. EDS mapping shows the exposed underlying substrate and the W-oxide smeared over the wear track.

steady-state wear are significantly higher at room temperature. In contrast, only minor differences are observed in the steady-state wear rates at 250, 500, and 700 °C, with the lowest wear occurring at 250 °C. At elevated temperatures, the running-in period is prolonged compared to room temperature. Following asperity fracture and debris generation, the wear particles are not removed from the contact zone as efficiently. Instead, as illustrated in Fig. 9, the debris becomes compacted into a thin oxide-based tribofilm, which contributes to the extended the duration of the running-in stage.

The first tribological contact occurs on the asperities or roughness present between the coating surface and the counterbody. The coefficient of friction for these contacts is relatively consistent, ranging from 0.4 to 0.6, regardless of temperature, with the highest initial COF being observed at room temperature. Identifying the reason for this is difficult, but it could be due to the lack of moisture on the coating surface or the formation of a thin oxide layer during the heating of the samples. Luo conducted a study on the origin of friction during the running-in period of TiAlN/VN multilayer films, where he discovered the presence of temporary hydro-oxygen-carbon-based absorbents that last for up to 20 cycles [25]. These absorbents increase the initial friction at room temperature, but heating the surface reduces their formation.

Nevertheless, the wear and the subsequent geometrical changes in the wear track present more significant contributions to the friction coefficient than the presence of adsorbents. Presented in all tested temperatures, the COF increases significantly over the next few hundred cycles. In Fig. 9, the SEM images at low test durations are presented. Similar to our previous study of magnetron sputtered TiAlN, an initial low friction coefficient is attributed to small-area asperity contact, which increases significantly with the progression of the sliding test [29]. The wear starts at the sites of the defects with localized breaking and spalling wear. These wear products remain near the defect, effectively increasing their surface area, thus decreasing the acting pressure from the load on these spots. Only the above surface part of the defects breaks and fragments, while the core incorporated in the coating usually remains intact. The wear debris is then subjected to further fragmenting and powdering.

Asperities in the wear track present the first sites of the coating oxidation as well as anchoring points for the collection of wear debris [29]. This applies to all types of growth defects in both magnetron-sputtered coatings and CAE coatings. Although the mechanical properties of individual growth defects may vary depending on seed composition, geometry, and size, the length of the running-in period at room temperature appears to depend primarily on the defect fracture rate and, consequently, on their density under tribological contact. The emission of droplets in the cathodic arc evaporation deposition process creates a much higher asperity density than in typical magnetron sputtered coatings. In sputtering the seeds for a defect growth are usually foreign particles that sporadically originate from substrates, cleaning procedures or previous depositions [42]. While the breaking and fragmenting mechanisms appear to be the same, the length of the RT running-in period in CAE coatings is much longer than in a magnetron-sputtered coating from [29].

In Fig. 9, squashed and fragmented asperities for RT and 250 °C are well seen after 300 cycles of tribological test. In contrast, for the test at higher temperatures, the debris seems incorporated in the semi-transparent tribological film in the wear scar (arrow in 500 °C, Fig. 9c). This indicates that the oxidized debris builds the tribological film between the coating and the counterbody at higher temperatures. This tribological film prolongs the running-in period. The formation of a debris layer through compaction has been observed in other

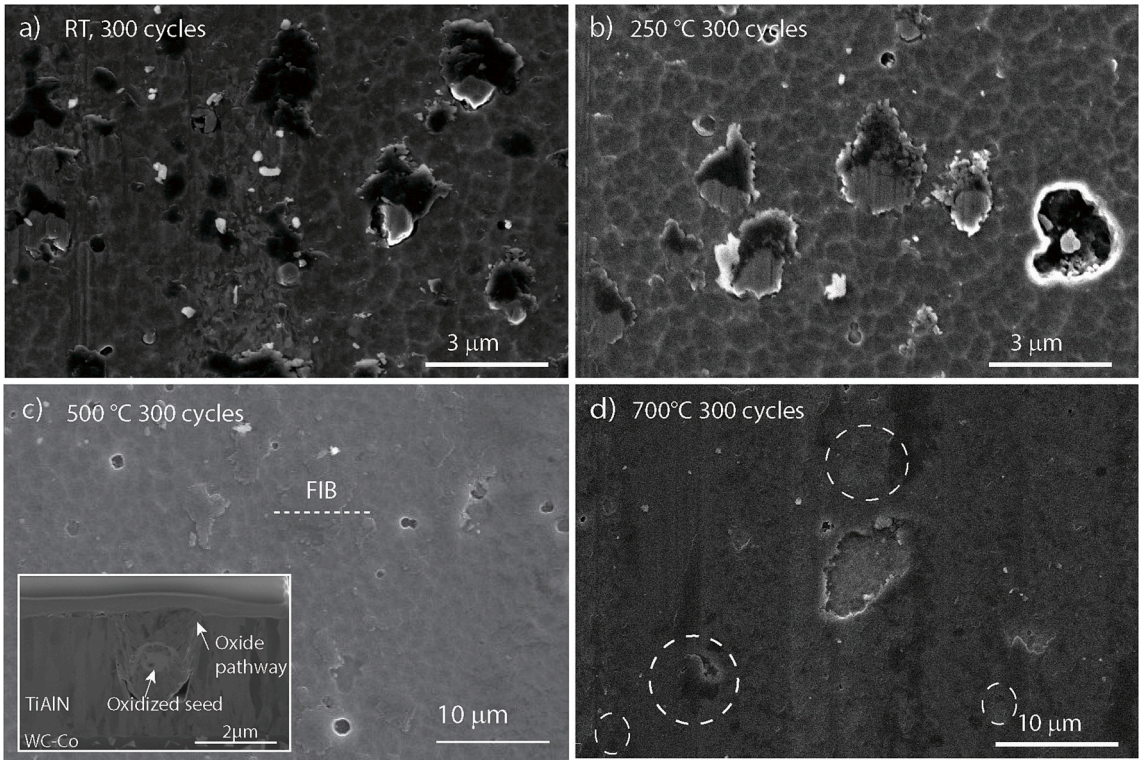

Fig. 9. SEM images of the worn surface after 300 cycles for (a) RT, (b) 250 °C, 500 °C, and (d) 700 °C test.

publications [25,43]. This process appears to occur more regularly at higher temperatures, while at ambient temperatures, the wear debris is removed from the wear track.

A FIB cross-section of a defect in the center of the wear track (Fig. 9c inset) reveals that the debris from the defect is oxidized and that the oxidation diffused into the coating via pinholes surrounding the defect. The pressed defect fragments are visible on the top of the coating surface. As the defects are usually not fully incorporated in the coating matrix, the pores at the site of the defect act as oxygen diffusion pathways. As shown in this case, the oxidation penetrated more than half of the coating thickness to the defect seed - a TiAl droplet, and oxidized some of the coatings along the pathway and the defect. This was not observed at lower temperatures where the oxidation is restricted to the contact zone only.

The defect spots in the center of the wear track are hard to distinguish at short cycle 700 °C tests (Fig. 9d). The absence of wear debris in the wear track indicates their incorporation into the tribological film. Selected defect spots are encircled in Fig. 9d. Larger holes form at the shallow site of growth defects, promoting oxidative wear at their edges. It is unclear how exactly defects contribute to the length of the running-in period, but it is evident from our tests that the running-in period during high-temperature operation depends not only on the density of defects but also on the rate at which the tribological film builds up, with an active role of defect debris in this build-up.

As already mentioned the breaking of growth defects and the initial appearance of the tribological film in the area of contact between two surfaces happens very quickly and results in significant changes in the shape and chemistry of the worn surface. As a result, the wear rate is high for the first couple of hundred cycles (Fig. 10a). The highest for room temperature tests. The average wear per cycle is higher than 1500 μm^3/cycle in the running-in period and drops in approximately 2000 cycles to 1000 μm^3per cycle at the end. At higher test temperatures the wear is much smaller, being the smallest at 250 °C for all the test lengths. At the transition from the running-in period to the steady state COF, the entrapped particles in the contact and the geometrical changes on the counterbody plow into the coating/tribo film surface. Significant abrasion marks that extend over the entire diameter of the tribological wear track can be seen in Figs. 4, 6, and 7. The COF experiences maxima at the highest density of these abrasions. At this point, the COF exhibits a frictional hump as the wear track smooths out with continuous sliding, but only for the tests conducted at elevated temperatures.

For the tests conducted at room temperature, the emergence of much shallower micro-abrasion marks with scattered roll-like debris produces a continuous COF transition to steady-state friction. Although the exact origin and mechanism of roll-like debris formation are not entirely understood, previous studies confirm the simultaneous appearance of micro-abrasion marks and roll-like debris in ambient room temperature ball-on-disc tests in mild wear conditions, mainly when tested against Al_2O_3 or WC-Co [44–46]. This suggests that the debris may have a component of the surrounding environment, such as oxygen or hydroxyl ions [44]. We can conclude that the roll-like debris does not promote lower COF, as they emerge in tests with the highest friction coefficient and wear.

Wear is the highest at room temperature (3D profiles presented in Supplementary S4). The initial wear at 250 °C is more than four times lower than at room temperature. Considering only the high-temperature measurements, wear exhibits a slight increase between 250 °C and 700 °C. Although elevated temperatures reduce the mechanical properties of the coating and thereby promote wear, the wear levels remain substantially lower than those observed at room temperature. Other researchers also report smaller wear with increasing temperature [47]. The wear stabilizes when the coefficient of friction enters the steady state period, which happens after 2000 cycles at room temperature and after 10,000 cycles at 250 °C and 30,000 cycles between 500 and 700 °C. Similar elongation of the running-in period with the temperature was reported for filtered CAE coatings [48]. The measured minimal wear after 140,000 cycles in the 250 °C tests was less than 10 μm^3per cycle. However, the wear in the longest 700 °C test is higher than the one presented, as the whole wear track is covered with up to 300 nm of oxidized substrate material.

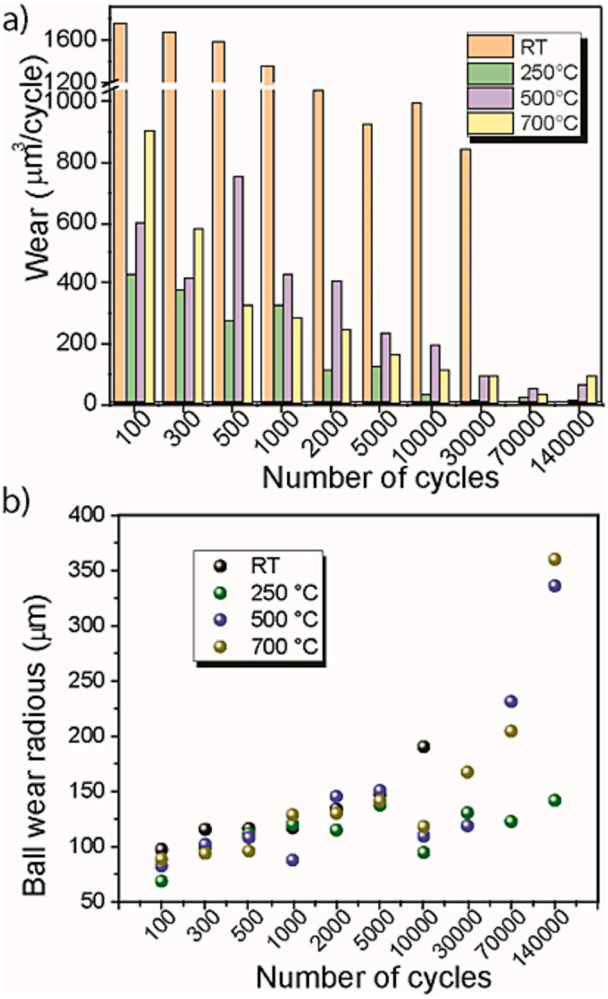

Fig. 10. (a) Wear rate data for all test lengths and temperatures; (b) Al_2O_3 ball wear radius for selected experiments at elevated temperature.

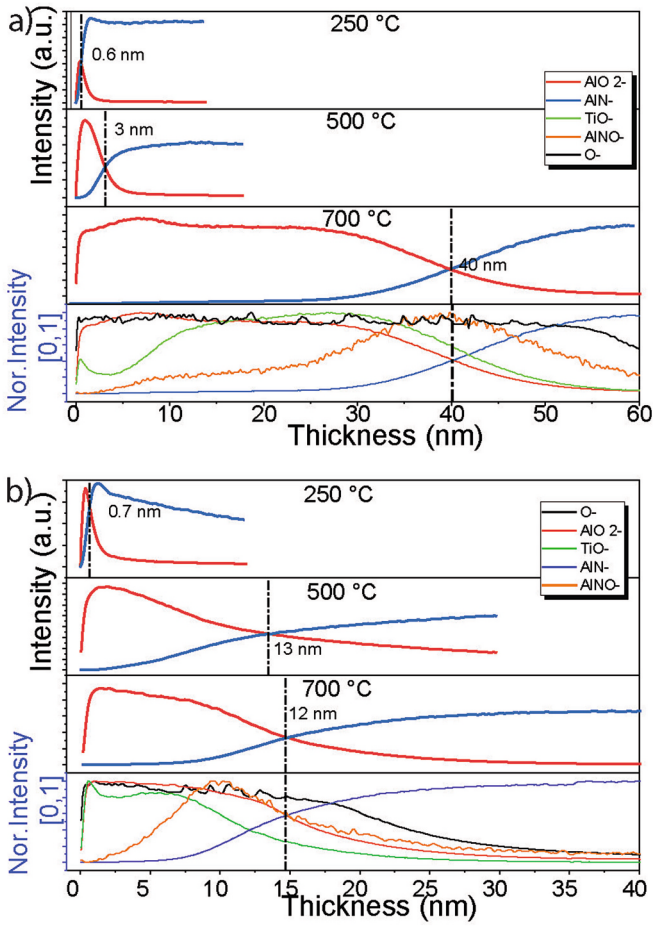

Fig. 11. (a) ToF-SIMS depth profiles on the coating surface outside the wear tracks and (b) in the wear tracks.

The temperature influences the wear of the counterbody as well (Fig. 10b). While we only measured the radius of the wear scar, it indicates that the ball wear at similar test lengths is increased above 500 °C, especially at longer tests (Supplementary S5). The drop of Al_2O_3 hardness at these temperatures is significant and can influence the wear and contact pressure distribution on the coating [49].

At elevated temperatures, the AlTiN coating forms a tribological film that affects both the coefficient of friction and wear, leading to low wear and confirming its protective properties. To measure the thickness of the oxide layer on the wear track, we used the Time-of-Flight Secondary Ion Mass Spectrometry (ToF-SIMS) method (Fig. 11). Applying this method, one can analyze the depth distribution of specific elements or species as a function of the etching time performed by a Cs-ion beam. We determined the thickness of the oxide film by observing the specific species that were etched from the wear track and the regions outside the wear track. The AlO_2^- and AlN^- ions were followed as a function of depth. The depth where these intensities intercept was determined as the oxide film thickness. The analyzed area in the wear track was 50 × 50 μm. Fig. 11a presents the SIMS depth profiles of oxide layers in an area outside the wear track, while in Fig. 11b, the SIMS depth profiles are presented from the wear track. The estimated thicknesses of the oxide layers are shown in SIMS depth profiles in Fig. 11.

At 250 °C and 500 °C, oxidation outside the wear track is minimal, resulting in oxide thicknesses of only 0.6 nm and 3 nm, respectively. However, at 700 °C, the sample changed color due to increased oxide growth. The measured thickness of the oxide layer from the SIMS depth profile was found to be 40 nm for this sample.

This demonstrates the AlTiN coating excellent oxidation properties at moderate to high temperatures. Although the thickness was determined based on the intensities of AlO^- and AlN^- ions, the actual oxide layer comprises also other species and elements. If the intensities of the other participating ions in the SIMS depth profile are normalized, it can be observed that the oxide layer consists mainly of Al-oxide (Al_2O_3) on top, and it starts to mix with Ti-oxide and Al-oxynitride at the interface with the undamaged nitride coating. It should be noted that the measured intensities of these ions are much lower than that of AlO_2^-. Nevertheless, the oxidation layer outside the wear track is very similar to those obtained in separate oxidation studies where the top of the oxide scale is covered with Al_2O_3 and TiO_2 below [50]. Such a layer is formed by the outward diffusion of nitrogen with the simultaneous inward diffusion of oxygen into the coating [50]. The top Al_2O_3 layer is dense and thus slows down the diffusion, increasing the oxidation resistance of this coating. In the worn-out area, the formation of the oxide scale can be intensified by the frictional load on the coating, but the oxide layer is also continuously removed by sliding motion. The ToF-SIMS depth profiles from the worn-out area are presented in Fig. 11a. At a temperature of 250 °C, the mild tribological conditions are insufficient to build a thick oxide scale as the thickness is comparable to that outside the worn-out area. At temperatures of 500 °C and 700 °C, the oxide scale's thickness is just above 10 nm. This is significantly different from the values measured outside of the wear track. The increased oxide growth at 500 °C is attributed to the effects of sliding. It can be inferred that the thicknesses mentioned represent the stable oxide thickness, as any excess is removed due to the sliding motion caused by lower adherence

between Al_2O_3, TiO_2, and the underlying coating. The composition of the oxide scale is similar to the one measured outside the wear track, with the only difference being the intensity of the TiO^- ions as this peak shifts more toward the surface. While this alone is insufficient to claim that the composition of the oxide scale is different, instead that the top Al_2O_3 layer is removed by sliding. Reports of other groups are claiming that at higher temperatures, the TiO_2 starts to diffuse toward the surface disrupting the continuous growth of the Al_2O_3 and thus increasing the diffusion of oxygen [51].

Comparing oxide thickness with the wear, it has been found that a thinner oxide layer tends to have better mechanical integrity, resulting in lower wear. Delamination occurs at the maximum testing temperature due to oxygen diffusion to the substrate-coating interface. Although tribo-oxidation and subsequent removal of the layer can lead to the complete removal of the coating, defects embedded close to or at the coating-substrate interface can cause more rapid deterioration. Such a process is portrayed in Fig. 12. After undergoing 30,000 cycles at a temperature of 700 °C, the coated material showed no damage. During sliding, the defect tops were removed in the initial sliding stage. In some cases, where the defects are embedded more deeply in the coating matrix, cracks start forming around the defect due to high local pressure and coating mechanical degradation due to high temperature and oxidation. In Fig. 12 a large tungsten seed embedded in the coating and cracks formed beyond the size of the defect are depicted. Due to the high-temperature conditions, the detached coating and the tungsten seed oxidized utterly as presented in EDS maps. The oxidation did not penetrate to the substrate. With longer sliding distances, numerous spots of detached coating were found in different stages of degradation. Fig. 12b and c presents fully oxidized defects at different stages. In Fig. 12b, the oxidized defect is separated by less than 200 nm of coating from the substrate, and small cracks are visible in the coating near the defect. EDS analysis shows that the defect seed was a molten drop mainly consisting of aluminum. In Fig. 12c, oxidation has penetrated on the side of the defect to the substrate. Once the oxide front reaches the substrate, oxidation of the Co binder and WC phase occurs, forming oxides such as CoO and WO_3. The volumetric expansion and change in local mechanical properties are particularly critical under tribological contact, where mechanical loading on the oxidized area intensifies local stresses. The expansion imposes high compressive stresses within the oxide and tensile stresses in the surrounding coating. This combination of oxidation-induced expansion, applied load, and thermal mismatch led to partial detachment of the coating near the defect and subsequent cracking above the oxidized substrate, accelerating the coating oxidation process. This very localized phenomenon intensifies with further sliding, leading to larger coating sections delaminating as it was shown in Fig. 8 after 140,000 cycles.

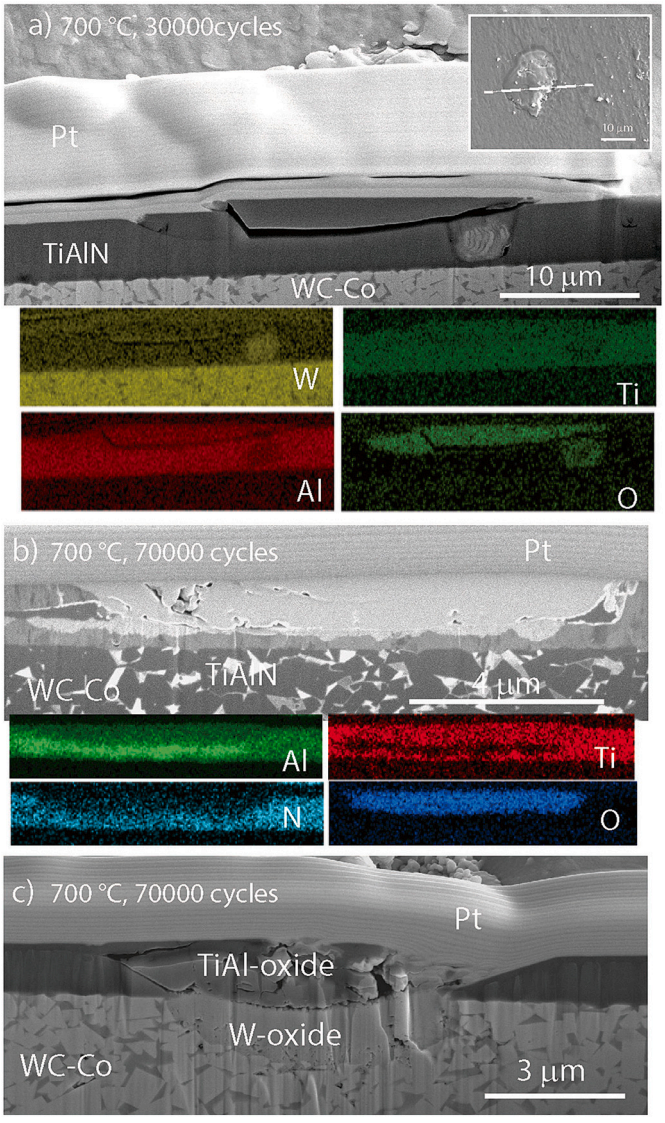

Fig. 12. SEM cross-sections through typical defects in the wear track after 700 °C tests. In (a) after 30,000 cycles, in (b) after 70,000 cycles where some coating remained beneath the defect, and in (c) also after 70,000 cycles at the site with substrate exposed and oxidized.

5. Conclusions

This study examined the high-temperature tribological properties of cathodic arc-deposited AlTiN hard coatings. Different range tribological tests at RT, 250, 500, and 700 °C revealed the role of growth defects in the contact and wear progression, eventually leading to coating detachment. Some general conclusions can be made:

- Wear is the highest at the beginning of sliding when the contact is not conformal, regardless of the temperature. The main mechanisms are the breaking and fragmentation of droplet defects at room temperature. The produced wear debris can cause abrasion of the coating before it is removed from the wear track. A larger surface contact area and high abrasion cause the COF to rise.
- At high temperatures, droplet defects play a significantly different role. They actively form a tribological film due to general mechanical degradation at elevated temperatures (lower HT hardness, plastic deformation), protecting the underlying coating. As the components yield under pressure, the resulting debris becomes integrated into the tribological layer, extending the running-in period. This process occurs more intensively at higher temperatures.
- At room temperature, the coatings steady-state wear mechanism is microabrasion. The formation of small oxide particles in the form of roll-like debris is visible.
- At elevated temperatures, tribological oxidation followed by the subsequent removal of the oxide layer serves as the primary mechanism. ToF-SIMS measurements revealed that oxidation is more intense within the wear track due to increased local temperatures. The maximum oxide layer thickness was observed at 500 °C and 700 °C, while at 250 °C the oxide thickness is about a nanometer. When the oxide reaches its critical thickness (couple of nm) it breaks off the coating and is removed by a counterbody, periodically. Sample temperature influences the kinetics of the oxide growth. Additionally, the oxide layer formed outside the wear track was the thickest at the highest temperature.
- Growth defects are the primary source for premature coating failure. At 500 °C and above, oxide formation was noticed at the sites of the droplet defects. This hindered the coating's mechanical stability,

leading to cracks and eventually to the oxidation of the underlying substrate. The coating started to delaminate from the substrate.

CRediT authorship contribution statement

Aljaž Drnovšek: Writing – original draft, Investigation, Funding acquisition, Formal analysis, Conceptualization. **Patrik Šumandl:** Writing – review & editing, Investigation, Data curation. **Žan Gostenčnik:** Writing – review & editing, Investigation, Data curation. **Janez Kovač:** Writing – review & editing, Formal analysis. **Miha Čekada:** Writing – review & editing, Funding acquisition.

Declaration of competing interest

The authors declare that they have no known competing financial interests or personal relationships that could have appeared to influence the work reported in this paper.

Acknowledgments

This work was supported by the Slovenian Research Agency (program P2-0082, project L2-50059). We also acknowledge funding from the European Regional Development Fund (CEEN Nanocenter): OP13.1.1.2.02.006 and the Center of electronic microscopy and microanalysis (CEMM) at the Jožef Stefan Institute.

Appendix A. Supplementary data

Supplementary data to this article can be found online at https://doi.org/10.1016/j.surfcoat.2025.132662.

Data availability

Data will be made available on request.

References

[1] V. Derflinger, H. Brändle, H. Zimmermann, New hard/lubricant coating for dry machining, Surf. Coat. Technol. 113 (3) (1999) 286–292.
[2] A. Hörling, et al., Mechanical properties and machining performance of Ti1−xAlxN-coated cutting tools, Surf. Coat. Technol. 191 (2–3) (2005) 384–392.
[3] K. Holmberg, A. Matthews, H. Ronkainen, Coatings tribology—contact mechanisms and surface design, Tribol. Int. 31 (1) (1998) 107–120.
[4] P. Panjan, A. Drnovšek, J. Kovač, Tribological aspects related to the morphology of PVD hard coatings, Surf. Coat. Technol. 343 (2017) 138–147.
[5] P. Panjan, et al., Surface density of growth defects in different PVD hard coatings prepared by sputtering, Vacuum 86 (6) (2012) 794–798.
[6] T. Leyendecker, et al., The development of the PVD coating TiAlN as a commercial coating for cutting tools, Surf. Coat. Technol. 48 (2) (1991) 175–178.
[7] W.D. Münz, Titanium aluminum nitride films: a new alternative to TiN coatings, J. Vac. Sci. Technol. A 4 (6) (1986) 2717–2725.
[8] J. Zhao, et al., Effects of Al content in TiAlN coatings on tool wear and cutting temperature during dry machining IN718, Tribol. Int. 171 (2022) 107540.
[9] A. Hörling, et al., Thermal stability of arc evaporated high aluminum-content Ti 1−x Al x N thin films, J. Vac. Sci. Technol. A 20 (5) (2002) 1815–1823.
[10] L. Chavee, et al., A mechanistic approach of oxidation resistance, structural and mechanical behaviour of TiAlN coatings, Appl. Surf. Sci. 586 (2022) 152851.
[11] H.D. Zhang, et al., Mechanical and thermal properties of AlN/Ti1-xAlxN (x = 0, 0.45 and 0.62) multilayers, Surf. Coat. Technol. 470 (2023) 129859.
[12] F. Esaka, et al., Depth profiling of surface oxidized TiAlN film by synchrotron radiation excited X-ray photoelectron spectroscopy, Surf. Sci. 377-379 (1997) 197–200.
[13] B. Grossmann, et al., High-temperature tribology and oxidation of Ti1−x−yAlxTayN hard coatings, Surf. Coat. Technol. 342 (2018) 190–197.
[14] H. Asanuma, et al., Impact of lanthanum and boron on the growth, thermomechanical properties and oxidation resistance of Ti–Al–N thin films, Thin Solid Films 688 (2019) 137239.
[15] L. Hultman, et al., Transmission electron microscopy studies of microstructural evolution, defect structure, and phase transitions in polycrystalline and epitaxial Ti1−xAlxN and TiN films grown by reactive magnetron sputter deposition, Thin Solid Films 205 (2) (1991) 153–164.
[16] P.V. Moghaddam, et al., High temperature tribology of TiAlN PVD coating sliding against 316L stainless steel and carbide-free bainitic steel, Tribol. Int. 159 (2021) 106847.
[17] V. Podgursky, et al., Dependence of the friction coefficient on roughness parameters during early stage fretting of (Al,Ti)N coated surfaces, Wear 271 (5–6) (2011) 853–858.
[18] S.M. Lee, et al., Friction drilling of austenitic stainless steel by uncoated and PVD AlCrN- and TiAlN-coated tungsten carbide tools, Int. J. Mach. Tools Manuf. 49 (1) (2009) 81–88.
[19] R. Rachbauer, et al., Temperature driven evolution of thermal, electrical, and optical properties of Ti–Al–N coatings, Acta Mater. 60 (5) (2012) 2091–2096.
[20] M.H. Staia, et al., High-temperature tribological characterization of commercial TiAlN coatings, J. Phys. Condens. Matter 18 (32) (2006) S1727–S1736.
[21] D. Jianxin, L. Aihua, Dry sliding wear behavior of PVD TiN, Ti55Al45N, and Ti35Al65N coatings at temperatures up to 600°C, Int. J. Refract. Met. Hard Mater. 41 (2013) 241–249.
[22] D.K. Devarajan, B. Rangasamy, K.K. Amirtharaj Mosas, State-of-the-art developments in advanced hard ceramic coatings using PVD techniques for high-temperature tribological applications, Ceramics 6 (1) (2023) 301–329, https://doi.org/10.3390/ceramics6010019.
[23] A.Y. Adesina, Tribological behavior of TiN/TiAlN, CrN/TiAlN, and CrAlN/TiAlN coatings at elevated temperature, J. Mater. Eng. Perform. 31 (8) (2022) 6404–6419.
[24] K. Holmberg, H. Ronkainen, A. Matthews, Tribology of thin coatings, Ceram. Int. 26 (7) (2000) 787–795.
[25] Q. Luo, Origin of friction in running-in sliding wear of nitride coatings, Tribol. Lett. 37 (3) (2010) 529–539.
[26] P.J. Blau, On the nature of running-in, Tribol. Int. 38 (11−12) (2005) 1007–1012.
[27] Peter J. Blau, Mechanisms for transitional friction and wear behavior of sliding metals, Wear 72 (1) (1981) 55–66.
[28] V. Podgursky, et al., Comparative study of surface roughness and tribological behavior during running-in period of hard coatings deposited by lateral rotating cathode arc, Wear 268 (5–6) (2010) 751–755.
[29] A. Drnovšek, et al., The influence of growth defects in sputter-deposited TiAlN hard coatings on their tribological behavior, Surf. Coat. Technol. 288 (2016) 171–178.
[30] M. Tkadletz, et al., The effect of droplets in arc evaporated TiAlTaN hard coatings on the wear behavior, Surf. Coat. Technol. 257 (0) (2014) 95–101.
[31] Q. Luo, et al., TEM-EELS study of low-friction superlattice TiAlN/VN coating: the wear mechanisms, Tribol. Lett. 24 (2) (2006) 171–178.
[32] Q. Luo, Temperature dependent friction and wear of magnetron sputtered coating TiAlN/VN, Wear 271 (9) (2011) 2058–2066.
[33] M. Fallqvist, M. Olsson, The influence of surface defects on the mechanical and tribological properties of VN-based arc-evaporated coatings, Wear 297 (1–2) (2013) 1111–1119.
[34] P. Panjan, et al., Growth defect density in PVD hard coatings prepared by different deposition techniques, Surf. Coat. Technol. 237 (2013) 349–356.
[35] Y.H. Chen, et al., Enhanced thermal stability and fracture toughness of TiAlN coatings by Cr, Nb and V-alloying, Surf. Coat. Technol. 342 (2018) 85–93.
[36] P.H. Mayrhofer, et al., Microstructural design of hard coatings, Prog. Mater. Sci. 51 (8) (2006) 1032–1114.
[37] Y.X. Xu, et al., Thermal stability and oxidation resistance of V-alloyed TiAlN coatings, Ceram. Int. 44 (2) (2018) 1705–1710.
[38] A. Drnovšek, et al., Correlating high temperature mechanical and tribological properties of CrAlN and CrAlSiN hard coatings, Surf. Coat. Technol. 372 (2019) 361–368.
[39] J. Pujante, et al., High temperature scratch testing of hard PVD coatings deposited on surface treated tool steel, Surf. Coat. Technol. 254 (2014) 352–357.
[40] K. Chang, et al., Friction and wear properties of TiAlN coated tools with different levels of surface integrity, Ceram. Int. 48 (4) (2022) 4433–4443.
[41] B. Biswas, et al., Effect of chamber pressure on defect generation and their influence on corrosion and tribological properties of HIPIMS deposited CrN/NbN coatings, Surf. Coat. Technol. 336 (2018) 84–91.
[42] P. Panjan, et al., Review of growth defects in thin films prepared by PVD techniques, Coatings 10 (5) (2020) 447.
[43] B. Biswas, et al., Effect of substrate bias voltage on defect generation and their influence on corrosion and tribological properties of HIPIMS deposited CrN/NbN coatings, Surf. Coat. Technol. 344 (2018) 383–393.
[44] Z. Zhou, et al., The role of the tribofilm and roll-like debris in the wear of nanoscale nitride PVD coatings, Wear 263 (7–12) (2007) 1328–1334.
[45] Z. Zhou, et al., Wear and friction of TiAlN/VN coatings against Al2O3 in air at room and elevated temperatures, Acta Mater. 58 (8) (2010) 2912–2925.
[46] A. Drnovšek, et al., The influence of surrounding atmosphere on tribological properties of hard protective coatings, Surf. Coat. Technol. 267 (2015) 15–20.
[47] M. Pfeiler, et al., Arc evaporation of Ti–Al–Ta–N coatings: the effect of bias voltage and Ta on high-temperature tribological properties, Tribol. Lett. 30 (2) (2008) 91–97.
[48] W.-Y. Lee, et al., Effect of defects on wear behavior in ta-C coating prepared by filtered cathodic vacuum arc deposition, Diam. Relat. Mater. (2020) 105, https://doi.org/10.1016/j.diamond.2020.107789.
[49] M. Rebelo de Figueiredo, et al., Nanoindentation of chemical-vapor deposited Al2O3 hard coatings at elevated temperatures, Thin Solid Films 578 (2015) 20–24.
[50] P. Panjan, A. Drnovšek, G. Dražić, Influence of growth defects on the oxidation resistance of sputter-deposited TiAlN hard coatings, Coatings 11 (2) (2021) 123.
[51] Z.B. Qi, et al., Relationship between tribological properties and oxidation behavior of Ti 0.34 Al 0.66 N coatings at elevated temperature up to 900 °C, Surf. Coat. Technol. 231 (2013) 267–272.